Version of Record: https://www.sciencedirect.com/science/article/pii/S0379711219306204
Manuscript_76cf0090a047f192d82b156e9a0af591

Dual Frequency Comb Spectroscopy of Solid Fuel Pyrolysis and Combustion: Quantifying the Influence of Moisture Content in Douglas Fir

A.S. Makowiecki, J.E. Steinbrenner, N.T. Wimer, J.F. Glusman,

C.B. Lapointe, J.W. Daily, P.E. Hamlington, G.B. Rieker

Department of Mechanical Engineering, University of Colorado Boulder

1111 Engineering Dr, Boulder, CO 80309, USA

Abstract

As the fire research community develops multi-scale models to predict the spread of wildland fires, there is a need for well-controlled, small-scale experiments which provide benchmark data and fundamental understanding of the effects of key parameters on the combustion of wildland fuels. Here, we implement a unique suite of non-intrusive, quantitative diagnostics that simultaneously measure mass loss, surface temperature, *in situ* gas temperature and water vapor concentration, including the first implementation of dual frequency comb spectroscopy for the study of solid fuels. As a demonstration, we examine the effect of fuel moisture content on the burning of Douglas fir wood samples that are ignited under constant radiative heat flux from a cone calorimeter to provide benchmark data for multi-scale models. Peak flame temperatures 3 mm above the sample surface measured with the dual frequency comb laser spectrometer are in excess of 1200 K. The flame temperature decreases by over 150 K as fuel moisture content increases from 0.7% to 40%. This work demonstrates a platform for simultaneous, quantitative measurements of well-controlled small-scale experiments which provide benchmark data for the development of advanced modeling and simulations capable of capturing the complex physics present in wildland fire systems.

© 2020 published by Elsevier. This manuscript is made available under the Elsevier user license
https://www.elsevier.com/open-access/userlicense/1.0/

***Keywords**:* wildland fire, flame temperature, cone calorimeter, solid fuel ignition, dual frequency comb spectroscopy

1. Introduction

Understanding and predicting wildland fire spread continues to be a key goal for the fire community. The complexity of wildland fires has given rise to a wide variety of experimental and computational approaches aimed at different aspects of fire spread processes [1–4]. In particular, developing wildland fire simulations with predictive capabilities requires fundamental understanding of the factors that influence the combustion, as well as experimental data that can serve as a benchmark during model development. Large-scale real wildland fire burn experiments provide the most realistic conditions, yet they also contain the largest number of uncontrolled variables and boundary conditions, which hinders their use for model development [4]. Small-scale experiments, on the other hand, allow for control and isolation of particular variables and repeat measurements. While these data necessarily simplify the problem, they can be used to identify key variables that drive flame spread processes at small scales and can serve as building blocks for the development of complex multi-scale models [5]. For example, modern computational simulations can cover length scales encompassing approximately three orders of magnitude, and can also incorporate sub-grid-scale models derived from even higher-resolution simulations with detailed chemical kinetics. By benchmarking high-resolution simulations against well-controlled small-scale experiments, the fidelity of large-scale models can be improved [6]. In this study, we describe a new diagnostic suite and experimental system to provide small-scale benchmarking information for solid fuel pyrolysis and combustion, with a first demonstration for the important variable of fuel moisture content.

Specifically, we implement a diagnostic platform to perform simultaneous *in situ* mass loss, optical imaging, surface temperature, laser-based gas temperature, and water vapor concentration measurements under a carefully controlled cone calorimeter to study the pre- and post-ignition behavior of radiatively heated samples.

The thermal diagnostics are non-intrusive. Surface temperature is measured with a calibrated infrared imaging camera. Simultaneous gas-phase temperature and water vapor concentration are measured with near-infrared frequency comb laser absorption spectroscopy [7], which is implemented here for solid fuel pyrolysis and combustion for the first time. Gas-phase temperature in wildland fires is often measured with thermocouples [8–13], with results varying widely depending on fuel type and condition, location in the flame, and many other variables. However, as stated in [14], "...temperatures from wildfire flames measured by thermocouples are not measurements of a single, well-defined quantity but an integration of heat transfer (through radiative and convective processes) from a mixture of gases, liquids and solids with a range of emissivities." The sensitivity of a thermocouple to radiation fluxes can change throughout its lifetime, particularly if the surface of the thermocouple is degraded or fouled due to smoke and elevated temperature. Additionally, the presence of the thermocouple or other probe can perturb the flow around the measurement, increasing the measurement uncertainty. Here, we instead rely on frequency comb laser absorption spectroscopy, which measures gas temperature by probing molecular energy levels of gases in the flow with light of different wavelengths. The experiment thus demonstrates a unique integration of traditional and state-of-the-art quantitative diagnostics and testing techniques that enable this and many future solid fuel combustion research studies. By performing concurrent measurements of many parameters under small-scale controlled conditions, we can identify correlations between these parameters and provide benchmarks for detailed modeing that become part of high-resolution computational fluid dynamics simulations [15–17]. In particular, Glusman *et al.* has used the experimental results presented here to inform a reduced-order chemical kinetic model for the pyrolysis behavior of Douglas fir [18].

As an example demonstration of the experimental platform, we study the influence of fuel moisture content on pyrolysis and combustion of wood samples. Fuel moisture content is a key variable in wildland fire spread because wood is hygroscopic, and its moisture content is quickly impacted by recent weather and relative humidity. Decreasing moisture content is known to cause an increase in wildland fire intensity and spread. Yet the number of quantitative experiments that provide the level of detail necessary for benchmarking high-resolution computational simulations is small. Thus, while the broad literature on fuel

moisture content is vast, we focus our review on investigations of moisture content of fuels that contain carefully controlled small-scale experiments and quantitative diagnostics. In particular, McAllister *et al.* studied the impact of fuel moisture content, heat flux, and air velocity parallel with the sample surface on the critical mass flux (flux just prior to ignition) of poplar samples, thus isolating the impact of convective heating on the samples [19]. Atreya *et al*. performed a similar investigation, studying the ignition behavior of Douglas fir as a function of air velocity, moisture content, and incident heat flux. It was determined that even with relatively dry samples, water vapor is the leading contributor to pre-ignition mass loss rate. Moghtaderi et al. performed a similar investigation using a cone calorimeter and computational models to investigate the ignition characteristics of dry and moisture conditioned wood samples [21], ultimately deriving an equation for predicting ignition temperatures taking into account external heat fluxes and fuel moisture contents. Harada *et al.* included an extensive investigation into the post-ignition mass flux for several fuel types and heat fluxes [22], concluding that density was the strongest indicator of fuel flammability. While Harada *et al.* did not investigate moisture content, the similarities in the experimental setup between Harada *et al.* and the current study make for an interesting point of comparison.

It is important to note the water vapor released during biomass combustion is driven by two processes; water produced from the thermal degradation of the wood during pyrolysis, and water which is not chemically bound to the wood and is emitted via evaporation [23,24]. While it is difficult to decouple these production methods, by varying fuel moisture content, the proportions of water vapor emitted from each source, particularly prior to combustion, is also varied.

The experiments here build on the work of the previous researchers to create a highly controlled dataset that provides multiple simultaneous targets for computational and kinetics models [18], including the important parameter of time-resolved gas-phase temperature both pre- and post-ignition.

2. Experimental Design

2.1. Mass Loss Calorimeter

A mass loss cone calorimeter from Fire Testing Technology Ltd., similar to the devices in [22,25], uniformly heats the samples and measures mass loss. The heat flux distribution across the plane of the sample surface was characterized with a water-cooled heat flux meter provided by GBH International. By translating the heat flux meter across the plane corresponding to the sample surface, the heat flux is found to be uniform to within 16% of the maximum (which occurs at the center) along the 12-cm sample length. The mass loss calorimeter contains a load cell, shown in Figure 1. The load cell post extends through a clearance hole in the purge system box in Figure 1, where it is attached to the sample platform. The load cell was calibrated with a 250 g calibration mass before testing. Dessicated air flows into the purge system box which consists of an outer metal box of 12.5” x 6” x 2.75” with a smaller box set of 5” x 4.5” x 2.5” set into the center of the larger box, where the sample was placed on the load cell pedestal. The area between the boxes was covered with a fine wire mesh top through which the dried air permeated at approximately 0.03 m/s to purge the area around the sample. The box was filled with small beads to act as a manifold/diffuser to break up and distribute the entering flow. The slow flow can then be considered uniform and laminar with a calculated Reynolds number of 0.29 based on mesh dimensions, flow rates, and surface area. The dry air removes the background laser absorption signal associated with water vapor in the ambient air without perturbing the flow over the sample, as evidenced by a lack of measurable water vapor absorption in the spectrum above dry samples prior to heating.

A spark igniter extends past the edge of the purge box and hovers approximately 10 mm above the center of the sample, as shown in Figure 2a. A large voltage difference applied to the igniter produces a continuous ~5 Hz spark above the sample without locally heating the sample surface. To determine ignition time, ignition type, and flame dynamics, a Canon Rebel T6i DSLR camera records the sample throughout the test at 30 frames per second.

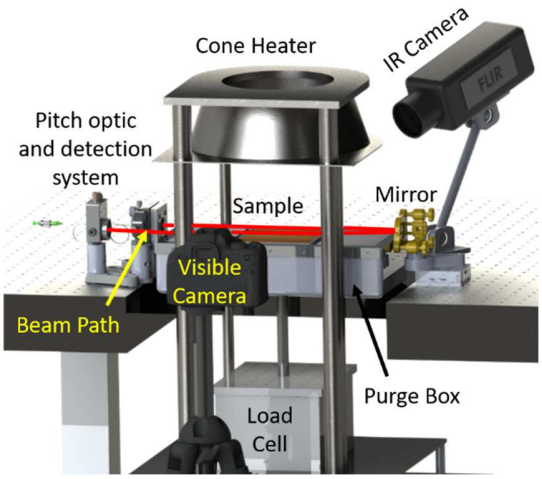

Figure 1: Experimental setup showing the configuration of the IR camera (surface temperature), laser beam path (gas-phase temperature and water vapor concentration), load cell (mass loss), and visual camera (optical images). Not shown is the heat flux gauge. The cone heater uniformly irradiates the sample, while the purge box surrounding the sample holder provides a uniform flow of dry air to purge portions of the laser beam path that are not over the sample.

2.2. Infrared Camera

A FLIR A655SC infrared camera is used to monitor the surface temperature of the samples throughout each trial. The camera was recently calibrated up to 2000°C by the manufacturer. Figure 2 shows images captured before ignition (Figure 2a) and after ignition (Figure 2b), including the location of the laser beam path above the sample. The surface temperature uncertainty is 2% of the reading, according to the manufacturer. The emissivity of the wood surface was assumed to be 0.95 for all trials. The change in emissivity of the samples due to surface charring was not accounted for in the calculation of temperature. We estimate that the change in emissivity increases the uncertainty of the measured surface temperature to approximately 4% of the measurement, prior to ignition. This is derived from the 4% change in measured temperature observed when the emissivity assumption is varied from 0.8 to 1, a larger variation than would be expected from wood [38]. During flaming combustion, the transmission through the flame is unknown

and the thermal radiation of soot from the flame is non-negligible, therefore surface temperatures post-ignition can be used for qualitative trends only.

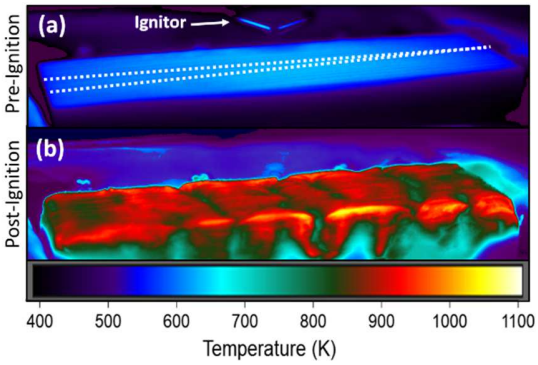

Figure 2: Infrared Camera image of sample surface temperature before (a) and after (b) ignition. The dashed lines in (a) correspond to the approximate location of the beam path over the sample and also indicate the path along which IR camera data is averaged for surface temperature measurements.

2.3. Dual Frequency Comb Absorption Measurements

Gas-phase temperature and water vapor mole fraction are measured using dual comb spectroscopy [7]. We have recently applied the dual comb spectrometer (DCS) for *in situ* species and temperature measurements in several turbulent environments, including stationary gas turbine exhaust systems [26], the open atmosphere [27], a rapid compression machine [28] and industrial burner flames [29]. A similar technique, Fourier transform infrared spectroscopy (FTIR), has previously been used to measure emissions from biomass burning in laboratory scale fires [30,31], though well outside the flaming regions. To the author's knowledge, the current work is the first demonstration of non-intrusive temperature and water concentration measurements recorded within a biomass flame.

In the dual-comb technique, broadband light from two optical frequency comb lasers is passed above the sample (at a height of 3 mm and beam diameter of 2.5 mm in these experiments) and interfered on a fast photodetector. The light is absorbed at specific wavelengths that correspond to transitions of water vapor molecules between discrete rotational-vibrational energy states that are allowed by quantum mechanics (see Figure 3). The absorption is quantified by heterodyne spectroscopy, where the measured

signal is captured in a 'beat' rf signal created by interfering two optical frequency combs. This technique down converts the optical signals to rf frequencies that can be measured by the detector. The magnitude of the absorption, and the unique temperature dependence of the absorption for each transition can be modeled using transition-specific parameters from databases such as HITRAN and/or experimental validations. Water vapor mole fraction and gas temperature are extracted by performing a non-linear least squares fit to minimize the residual between the measurement and the modeled absorption by varying the water mole fraction and temperature of the modeled absorption.

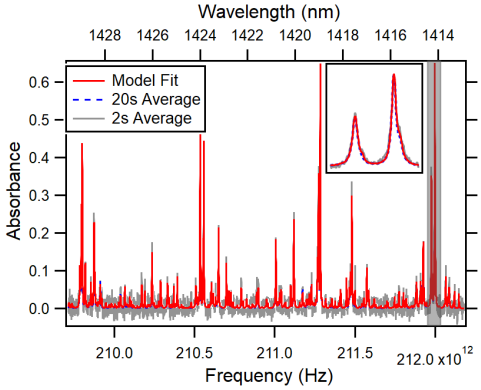

Figure 3: Example dual frequency comb absorption spectrum of water vapor absorption during flaming combustion. The data is fit with an absorption model to determine gas-phase temperature and water vapor mole fraction. Inset from area highlighted with grey box at 212 THz.

The systematic uncertainty introduced by the DCS instrument itself has been shown to be lower than 1% [32]. The dominant uncertainty associated with the measurement comes from the uncertainty of the absorption model used in the fit [33] and non-uniform temperature gradients in the experiment. In this case, the absorption model is generated using experimentally validated linestrengths, which describe the magnitude of an absorption feature, from Ref. [34]. The experimental linestrengths are augmented by air-broadening and pressure shift parameters from the HITRAN2012 database [35]. Broadening parameters describe how the width of the absorption feature will change based on the concentration of gases present in the system and the pressure shift parameter describes how the center wavelength of a feature will vary with pressure. CO_2-broadening parameters have not been characterized for all features within this bandwidth so

an approximation of $\gamma_{CO2} \approx 1.7\gamma_{air}$ from Ref. [36] with an assumed CO_2 mole fraction of 7% based on [37] was used to more accurately represent broadening conditions present in the system.

Non-uniform temperatures were minimized by using dried air to purge all sections of the beam path laying outside the perimeter of the wood sample, as discussed in Section 2.1. The measurement is fundamentally absorption weighted, meaning areas with increased water concentrations, like flames, are weighted more heavily when fitting for temperature, this minimizes the contribution from background absorption during temperature fits, particularly during flaming combustion. We estimate the total systematic uncertainty due to model and instrument uncertainty to be less than 3% for the gas-phase temperature and water vapor mole fraction measurements. Due to the nature of diffusion flames, and in some cases the presence of multiple separate flaming regions, the temperature and water vapor distribution of the gases within biomass flames are non-uniform. Since absorption measurements are inherently pathlength averaged the technique cannot capture a localized high temperature or concentration, but instead report an absorbanceweighted gas temperature and a pathlength-averaged mole fraction.

The dual frequency comb spectrometer used in this investigation spans approximately 1200 to 1800 nm with 200 MHz (0.0013 nm) measurement point spacing. A portion of the water vapor absorption bands near 1422 nm were used for this study. Spectra are recorded at 3.7 kHz, and averaged to 2 s before each fit to improve the signal-to-noise ratio (SNR). Figure 3 shows an example of a spectral fit recorded during flaming combustion. A fit of each 2-s spectrum leads to the time-resolved traces for H_2O vapor concentration and gas-phase temperature shown in Figure 4. It is important to note that our measurements of flame temperature represent a laser-beam-path average temperature recorded approximately 3 mm above the surface of the wood sample. The peak gas temperatures reported in the following sections signify the highest path-average temperature recorded at a location 3 mm above the surface of the wood sample for each trial.

DCS was selected over other diagnostic techniques for its rapid detection, coherent nature, and broad bandwidth. The coherent nature of DCS allows the beam to cover large distances, while the heterodyne detection removes the influence of thermal radiation from flames and hot surfaces.

Traditional tunable diode laser-based spectropscopic techniques are limited by a narrow frequency range, which requires multiple lasers at carefully selected wavelengths in order to measure multiple species and temperature. The broad bandwidth of DCS can provide for the simultaneous measurement of several molecular species absorbing within its detection bandwidth because each gas exhibits a unique absorption fingerprint. The broad bandwidth detection of DCS also increases the dynamic temperature range which can be quantified as it can target absorption features with different temperature sensitives. Compared with other broad-bandwidth spectroscopic techniques, the DCS technique enables measurement in transient conditions. For the same resolution, DCS can scan 1,000 times faster than FTIR systems.

3. Heat Transfer Model

To investigate the driving factors behind experimentally observed trends, a 3-dimensional finite element code was written in MATLAB using the thermal analysis PDE toolbox [39]. While more comprehensive models exist for this application [40–42], the simplified model allows parametric exploration of the observed trends. The samples are modeled as rectangular prisms with dimensions of 120x40x20 mm consistent with the actual sample sizes, and meshed with a uniform 0.5-mm grid spacing. The thermal properties of each sample (density, thermal conductivity and specific heat) are specified in the model. The density of the samples is calculated by dividing the measured mass of each sample by the volume prior to heating. The thermal conductivity (k) is defined as a function of moisture content and specific gravity based on measurements by Ref [43]. The temperature-dependent specific heat ($C_p(T)$) is calculated at each location and time step based on the empirical relationship introduced by Ref [43]. Convective heating on the top face of the sample is estimated by taking the ambient temperature to be the average air temperature above the samples prior to ignition, as measured by the DCS when background data was collected before each trial . The convection coefficient (h) is calculated using a heated flat horizontal plate approximation from [44] defined by Eq. (, where the Rayleigh number (Ra_L) is defined by Eq. (. The characteristic length (L) is defined as the surface area of the heated surface divided by the

perimeter. The sides of the sample are estimated to be adiabatic, because the energy loss from the sides of the sample is small compared with other heat transfer rates in the system, due to the small area for convection from the sides of the sample. This assumption was verified by running the model both with convective boundaries with h = 6 W/m^2 K and adiabatic and observing that these cases resulted in the same solution for temperature within 0.1 K. To account for radiative losses, the emissivity (ϵ) is kept at a constant value of 0.95, which is representative of a diffuse-gray absorber. The heat flux from the mass loss calorimeter is measured with the heat flux meter and is used as the heat flux boundary condition at the top face of the sample. The sample sits on a ceramic board during combustion, and the bottom face of the sample is modeled as an isothermal boundary condition. Final solutions are independent of this boundary condition as the wood samples can be considered thermally thick prior to ignition with a maximum Fourier number of 0.017.

$$h \approx \frac{k_{air} 0.54 Ra_L^{\frac{1}{4}}}{L} \tag{1}$$

$$Ra_L = \frac{g \rho_{air} \mathrm{C_p}}{\nu_{\mathrm{air}} \mathrm{k_{air}} \mathrm{T_{amb}}} (T_s(t) - T_{amb}) L^3 \tag{2}$$

To account for evaporative losses in the samples, the average measured mass flux out of the samples prior to ignition is assumed to consist only of water vapor. While the PDE toolbox does not include evaporation, the heat loss due to this evaporation was quantified by multiplying the latent heat of vaporization of water by the mass flux out of the sample for each moisture content case. The resulting heat loss by evaporation is subtracted from the constant heat flux imposed on the top surface of the sample by the cone heater.

4. Experimental Procedures

Samples of Douglas fir are cut into approximately 120x40x20 mm pieces and lightly sanded with 220 grain sandpaper to ensure uniform finishes on each sample. All samples are placed in an 85°C oven for several days until the mass of the samples no longer decreases with time. At the end of the bake-out period, the mass of each sample is recorded as the dry mass. Two separate batches of samples were burned 3 weeks apart. Batch 1 consisted of 14 samples divided into three moisture content 'groups'. Batch 2 consisted of 28 samples divided into 5 moisture content 'groups'. The details of the number of samples and their moisture contents are included in Table 1. All samples for a given moisture content group are soaked in distilled water for a set amount of time, then placed in airtight containers for approximately two weeks to allow the moisture to distribute evenly through the samples. During this time, the dry samples are stored in airtight containers with desiccant packets to prevent moisture re-absorption. All samples are weighed within 3 minutes of the experiment to determine the mass increase due to moisture absorption. Moisture content values are reported as the percentage increase in mass from the dry mass.

Table 1. Quantity and moisture content of Douglas fir samples tested.

	Batch 1 Samples		Batch 2 Samples	
Moisture "Group"	Average Moisture Content (%)	Quantity	Average Moisture Content (%)	Quantity
A	0.7 ± 0.02	5	0.69 ± 0.05	6
B			2.7 ± 0.17	5
C	7.71 ± 0.38	5		
D			11.39 ± 0.5	4
E	21.85 ± 0.37	3	21.5 ± 0.24	5
F			43.67 ± 1.98	6

After each sample is weighed, it is placed on the load cell with the grain orientated perpendicularly to the heat source, with the shutter system of the mass loss calorimeter (MLC) closed to prevent pre-heating

of the sample. All diagnostics are started and the MLC shutter is opened, exposing the sample to a heat flux of 21.9±1.7 kW/m^2. Within 10 s of opening the shutter the igniter pilot is switched on, creating a repetitive spark above the sample. After sustained flaming is achieved, the igniter is removed. Between Batches 1 and 2, the control system for the igniter failed, requiring a different voltage source to be used with the existing probe for subsequent tests. The shutter of the mass loss calorimeter remains open during flaming combustion to allow smoke to be exhausted from the environment. During flaming combustion, the mirror in Figure 1 is adjusted to compensate for beam steering induced by density gradients in the flame. After approximately 250 s of flaming combustion, the sample is extinguished.

5. Results and Discussion

5.1. Experimental Results

The results of simultaneous gas-phase temperature, surface temperature, water vapor mole fraction, mass loss, and mass flux measurements before and after sample ignition are shown in Figure 4 for representative samples with varying moisture content. The source of the water production pre-ignition is driven by two processes, evaporation and pyrolysis. While it is difficult to decouple the production source of the water vapor, it can be assumed that the proportion of water vapor produced from evaporation is increased as initial fuel moisture content is increased. For each experiment with low moisture content, the mass flux, gas temperatures, and water vapor mole fractions are relatively constant before ignition of the sample. This indicates a consistent rate of production of water vapor from pyrolysis and evaporation is occurring prior to ignition. Only the highest moisture content case (Figure 4c) shows a different trend, where an elevated water vapor mole fraction is observed initially due to the presence of a water film on the

surface of these samples, which were kept in the water bath until just prior to the experiment to achieve maximum moisture content. Comparing across fuel moisture contents, the pre-ignition mole fraction of water and pre-ignition mass flux are lowest for dry samples (MC group A) and elevated for higher moisture content samples (MC groups B through F), as expected. It should be noted that all of the samples were thermally-thick, and even the driest sample contained enough moisture to sustain evaporation until the point of ignition. These trends in moisture evolution may not apply to thermally-thin samples.

Sample ignition is marked by a steep increase in gas temperature that corresponds to the presence of large flames which cover the surface of the sample as the accumulated pyrolysis gases initially burn. Water vapor mole fraction, mass flux, and surface temperature also increase rapidly after ignition. The surface temperature of the sample remains elevated at a constant temperature following ignition, while the gas temperature only remains constant after ignition in the case of the driest sample (MC group A), where the gas temperature reaches and remains above 1200 K. For samples with moisture content above 20% (MC groups E and F), the gas temperature reaches a peak value above 1000 K just

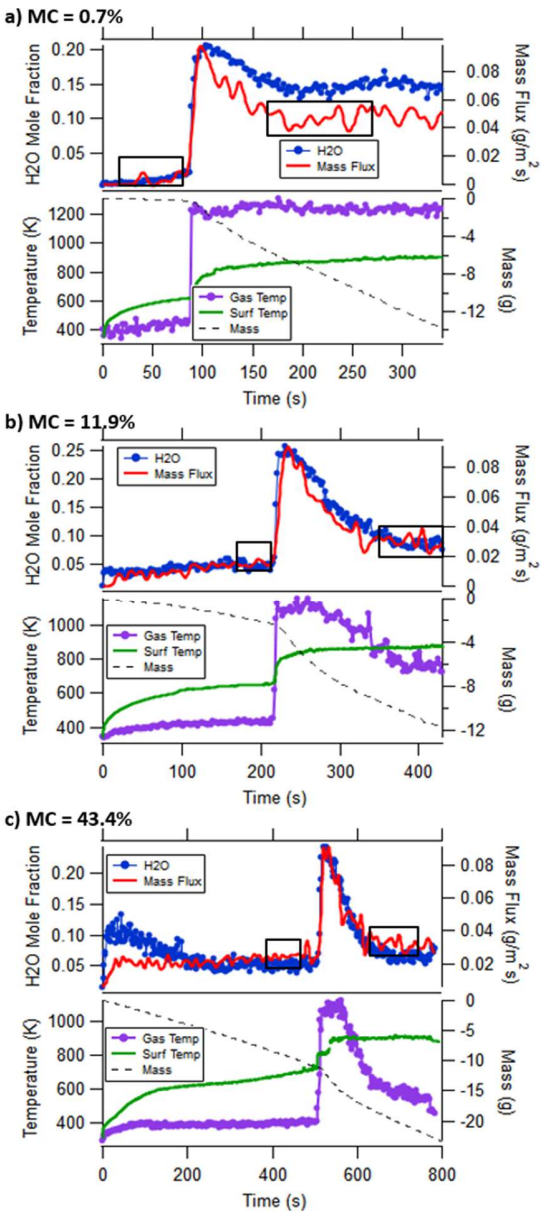

Figure 4: Representative plots of surface temperature, mass loss, mass flux, gaseous temperature and water mole fraction for three samples with varying moisture content: (a) 0.7% (b) 11.9% (c) 43.4%. All three cases were exposed to a radiative flux of 21.9±1. 7 kW/m2 and were piloted in the same manner. Note that the time axis is not consistent from panel to panel- higher moisture content fuels took much longer to ignite. The boxed points indicate the region of data which was averaged to calculate pre- and post-ignition mass flux for Figure 6.

after ignition and then decreases, with the decrease more pronounced and rapid with increasing moisture content.

These path-averaged temperature trends correlate well with visual observations of flame intensity and magnitude. Figure 6 shows images of the flames 30 s after ignition and 60 s after ignition. The qualitative flame intensity and size is greatly diminished by 60 s for the 21.5% and 40.8% MC samples (MC groups E and F), and only slightly diminished for the dry sample (MC group A).

There is strong correlation between the water vapor mole fraction and mass flux time histories, as shown in the upper panels of each subplot in Figure 4. Both water vapor mole fraction and mass flux peak after ignition and then decrease simultaneously, in agreement with the water vapor trends shown in Ref. [20]. The peak mole fraction of water vapor after ignition is a relatively consistent 0.20-0.25 for all cases and decreases post ignition. For the highest moisture content samples (MC group F), the water vapor concentration decreases rapidly as the cooler flames provide a reduced heat flux to the burning sample, while for the dry samples (MC group A), the water vapor concentration decreases somewhat before maintaining a higher steady-state concentration compared with the samples of higher moisture content.

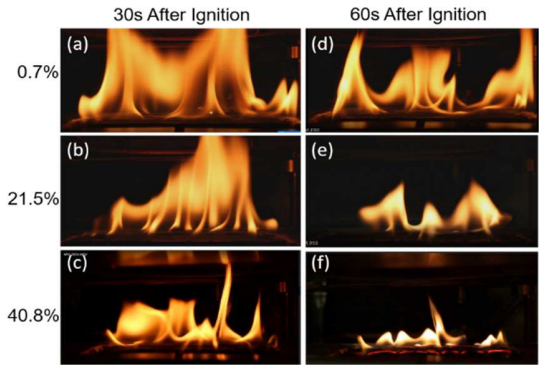

Figure 5: Flame structure for sample at 30 s post-ignition (a-c) and 60 s post-ignition (d-f), for three moisture content cases: 0.7% (a and d), 21.5% (b and e) and 40.8% (c and f). The flame qualitative intensity and magnitude is diminished for both higher moisture content samples 60 s after ignition.

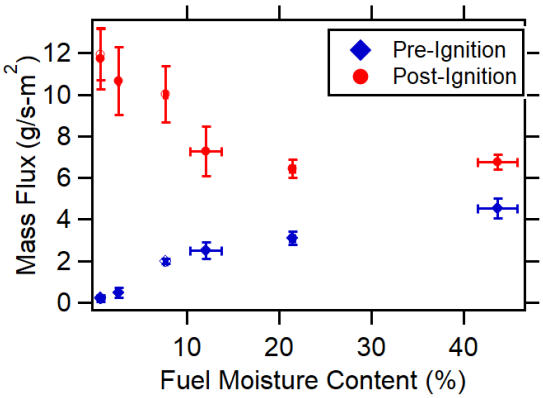

Figure 6: Mass flux before and after ignition as a function of sample moisture content. Mass fluxes represent the average of the time-resolved data encompassed by boxes in Figure 4. Data from samples in the same batch which were treated to achieve a similar moisture content were combined into each data point shown on this graph. The error bars represent the extents of variation between these samples for each average. Data from Batch 1 is represented by empty markers, while Batch 2 data is represented as solid markers.

This is consistent with the flame temperature and visual flame data, which show the flame weakening and developing more quickly into a patchwork of flame and surface smoldering for higher moisture content samples. The weaker combustion is accompanied by lower rates of mass loss. The lower rate of fuel consumption would be expected to produce less water vapor. To expand the application of these measurements, it would be useful to convert the measured mole fractions to species-specific mass fluxes from the surface. This would require an estimate of velocity and mixing at the surface of the wood sample, which could be accomplished through comparison to computational models or experimental measurements.

The time-to-ignition increases as the moisture content of the sample increases, consistent with previous studies [19,22,20]. This trend was consistent for each igniter configuration, but we do not quantify the ignition timing results because the ignition time depended on the igniter voltage source (and two different sources were used for the two batches of samples).

Figure 5 shows the effect of moisture content on the measured mass flux pre- and post- ignition. The mass fluxes shown are determined from an average of the measured mass flux data prior to ignition and after ignition (denoted by the black boxes in Figure 4). An average was used due to the sensitivity of taking the derivative of discrete data with noise. Despite the different igniter configurations, there is good agreement between the two trials. As the moisture content of the fuel increases, the pre-ignition mass flux increases. Given the correlation between water vapor mole fraction and mass flux discussed above, this result is consistent with a higher rate of water vapor leaving the sample. Above a fuel moisture content of approximately 12%, the pre-ignition mass flux no longer increases proportionally to the fuel moisture content. This observation agrees well with Moghtaderi *et al.,* who observed a similar trend during the combustion of Radiata pine, where the mass flux prior to ignition was relatively constant for samples at moisture contents greater than 10% [21]. Future detailed modeling will aid in the interpretation, but this could suggest that the rate of moisture leaving the sample becomes diffusion limited.

Conversely, the post-ignition mass flux decreases with increasing fuel moisture content, indicating that wet fuel is consumed at a slower rate than dry fuel. While one would expect this result, it is interesting that this trend plateaus for high fuel moisture content, so as the moisture content increases above 10-15%, there is no further reduction in post-ignition mass flux.

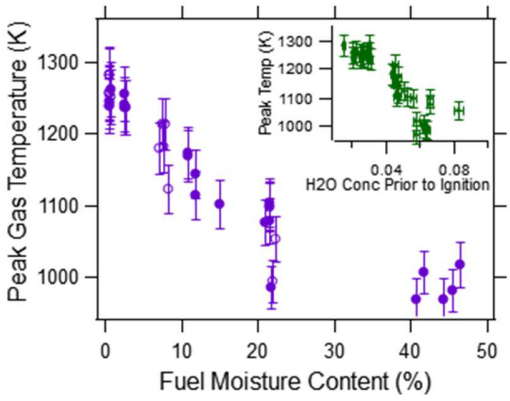

Figure 7: The effect of fuel moisture content on the peak gas temperature measured 3 mm above the sample surface. The inset shows the peak gas temperature data plotted as a function of the measured water vapor concentration in the gases above the sample just prior to ignition.

The peak flame temperature decreases with increasing fuel moisture content as shown in Figure 7. The peak temperature decreases from nearly 1300 K for dry fuel to ~1000 K for fuel with moisture content of 40%. For fuel moisture content below 20%, the decrease in temperature is proportional to moisture content with a slope that is found to be within 20% of another past study on pine [45]. As moisture content increases above 20%, the decrease in peak temperature is less significant. The higher pre-ignition water vapor concentration for fuels with more moisture content will serve to dilute the wood pyrolysis products and absorb energy during ignition and combustion. These results exhibit a similar temperature versus fuel moisture content trend reported for a Chemkin simulation of pyrolysis gases in an idealized opposing jet burner in Ref [24].

5.2. Model Comparison

The FEA model used in this study was developed to explore the surface temperature trends seen in the experimental data. Figure 8 shows the pre-ignition surface temperature of the samples prior to ignition in comparison to the calculated surface temperature from the MATLAB finite element analysis. Before accounting for evaporative losses, there is poor agreement between the model and the data (Figure 8 fine dashed lines). Once we incorporate the energy loss by mass flux due to evaporation, into the FEA model, there is good agreement between the model and the surface temperature measurements, with the exception of the highest moisture case (Figure 8 thick dashed lines). The data-model agreement suggests that energy absorption by evaporation significantly affects the surface temperature. In the highest moisture content case, the model does not capture all physics, and the data shows irregular behavior, indicated by the change in convexity occurring around ~20 s. This behavior is likely due to the presence of a liquid film on the surface of the sample discussed in Section 5.1, which is not accounted for in the simplified model.

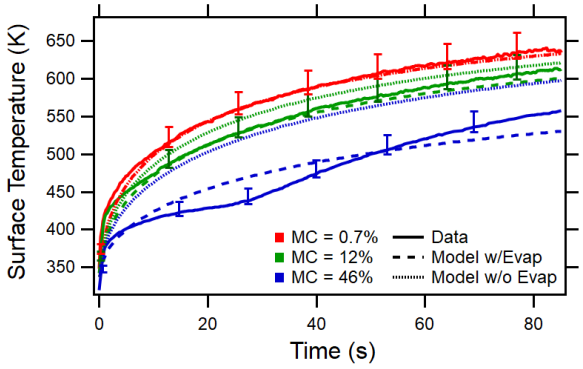

Figure 8: Comparison of measured surface temperature (solid lines) with modeled surface temperature with heat loss from evaporation (thick dashed lines) and without heat loss from evaporation (fine dashed lines) for the samples shown in Figure 4. Uncertainty bars indicate measured surface temperatures uncertainty for a range of surface emissivity from ε=0.8 to ε=1.

For all moisture contents, the surface temperature lines eventually appear to become noisier and the modeled temperature begins to deviate from the measured temperature. This is due to charring and cracking on the surface of the samples. When this occurs, the assumptions of uniform properties throughout the sample and losses dominated by evaporation begin to break down. Evaporative losses delay this transition

to charring for higher moisture contents. For higher fidelity at longer time intervals, pyrolysis kinetics should be incorporated in the future into the FEA model, such as the models demonstrated by [40,41,46].

6. Conclusions

We demonstrate a new diagnostic suite for small-scale biomass pyrolysis and combustion experiments that combines traditional approaches and modern laser-based sensing to provide the controlled boundary conditions and multi-parameter measurements that are necessary for developing and validating high-resolution chemical kinetic and computational fluid dynamic models.

As a first demonstration, we apply the diagnostic suite and cone calorimeter experimental platform to the pyrolysis and combustion of Douglas fir with varying moisture content. Through simultaneous measurements of sample mass loss, surface temperature, gas temperature and water vapor concentration, this study provides insight into the pre- and post-ignition behavior of Douglas fir wood subject to a constant imposed heat flux. A simple finite element analysis model was developed to explore surface temperature trends as a function of moisture content. When compared to experimental surface temperature measurements, the model results indicate evaporative losses from the samples account for lower surface temperatures and delayed temperature increases seen in higher moisture content cases.

As moisture content in the sample rises, pre-ignition mass fluxes increase due to increased evaporation from the wet sample. The mass flux and water vapor concentration above the sample surface are observed to be highly correlated, which is expected prior to ignition if water evaporation dominates the mass flux. After ignition, this correlation is less easily interpreted, since water vapor could appear both from evaporation and as a product of combustion. Additionally, post-ignition mass fluxes are smaller for samples with high water content, because the wet samples burn more slowly. However, both the increase in pre-ignition mass flux and the decrease in post-ignition mass flux appear to asymptote (toward similar values) as moisture content increases. These trends could be related to diffusion limits of water vapor through the wood and/or the energy balance of the sample.

Upon initial ignition, peak gas temperatures above 1000 K are observed for all samples, regardless of moisture content, at a height of 3 mm above the sample. Lower moisture content fuels exhibit the highest gas temperatures, in excess of 1200 K, and sustain these high temperatures after ignition. For moist samples, we observe a decrease in the peak gas temperature after ignition. This temperature decrease occurs more rapidly and is more pronounced for wetter samples, and correlates well with diminished mass flux and visual flame intensity.

This study introduces the first dual frequency comb spectroscopy of biomass burning in order to make non-intrusive measurement of gas temperature and species concentration. In the near future, we plan to extend the measurement capabilities using new mid-infrared wavelength frequency comb sources that are able to access the absorption signatures of H_2O, CO, CO_2, Formaldehyde, and various hydrocarbons simultaneously. Also, the application of a first law energy balance with major simplifying assumptions was used here for first order determination of the primary factors influencing initial heating behaviors, but did not fully explain the surface temperature trends on high moisture content samples (>40%). A more detailed analysis of the transport mechanisms and chemical kinetics in the system can now be performed with the benchmark data provided by these experiments. While this experimental necessarily simplified biomass ignition to solid thermally thick samples, it is widely acknowledged that thermally thin materials such as leaves and small branches are largely responsible for fire spread. Future experiments investigating emissions from thermally thin samples are currently being developed.

Acknowledgments

This research was supported by SERDP under grant W912HQ-16-C-0026 as project number RC-2642. The frequency comb laser diagnostics were developed under National Science Foundation Grant Number CBET 1454496 and the U.S. Department of Energy Advanced Research Projects Agency-Energy (ARPA-E) Award Number DE-AR0000539. The views and opinions of authors expressed herein do not necessarily state or reflect those of the United States Government or any agency thereof.

References

[1] J.J. Sharples, Review of formal methodologies for wind–slope correction of wildfire rate of spread, Int. J. Wildland Fire. 17 (2008) 179–193. https://doi.org/10.1071/WF06156.
[2] M.A. Finney, J.D. Cohen, J.M. Forthofer, S.S. McAllister, M.J. Gollner, D.J. Gorham, K. Saito, N.K. Akafuah, B.A. Adam, J.D. English, Role of buoyant flame dynamics in wildfire spread, Proc. Natl. Acad. Sci. 112 (2015) 9833–9838. https://doi.org/10.1073/pnas.1504498112.
[3] F. Morandini, X. Silvani, Experimental investigation of the physical mechanisms governing the spread of wildfires, Int. J. Wildland Fire. 19 (2010) 570–582. https://doi.org/10.1071/WF08113.
[4] A.L. Sullivan, Wildland surface fire spread modelling, 1990–2007. 2: Empirical and quasi-empirical models, Int. J. Wildland Fire. 18 (2009) 369–386. https://doi.org/10.1071/WF06142.
[5] D. Morvan, Physical Phenomena and Length Scales Governing the Behaviour of Wildfires: A Case for Physical Modelling, Fire Technol. 47 (2011) 437–460. https://doi.org/10.1007/s10694-010-0160-2.
[6] J.-L. Dupuy, R.R. Linn, V. Konovalov, F. Pimont, J.A. Vega, E. Jiménez, Exploring three-dimensional coupled fire–atmosphere interactions downwind of wind-driven surface fires and their influence on backfires using the HIGRAD-FIRETEC model, Int. J. Wildland Fire. 20 (2011) 734–750. https://doi.org/10.1071/WF10035.
[7] I. Coddington, N. Newbury, W. Swann, Dual-comb spectroscopy, Optica. 3 (2016) 414–426. https://doi.org/10.1364/OPTICA.3.000414.
[8] J.D. Walker, B.J. Stocks, Thermocouple errors in forest fire research, Fire Technol. 4 (1968) 59–62. https://doi.org/10.1007/BF02588607.
[9] T. Marcelli, P.A. Santoni, A. Simeoni, E. Leoni, B. Porterie, Fire spread across pine needle fuel beds: characterization of temperature and velocity distributions within the fire plume, Int. J. Wildland Fire. 13 (2004) 37–48. https://doi.org/10.1071/WF02065.
[10] C.W. Philpot, Temperatures in a Large Natural-Fuel Fire, Pacific Southwest Forest and Range Experiment Station Berkeley CA., 1965. http://www.dtic.mil/docs/citations/AD0644700 (accessed November 30, 2017).
[11] B.W. Butler, J. Cohen, D.J. Latham, R.D. Schuette, P. Sopko, K.S. Shannon, D. Jimenez, L.S. Bradshaw, Measurements of radiant emissive power and temperatures in crown fires, Can. J. For. Res. 34 (2004) 1577–1587. https://doi.org/10.1139/x04-060.
[12] P.A. Santoni, A. Simeoni, J.L. Rossi, F. Bosseur, F. Morandini, X. Silvani, J.H. Balbi, D. Cancellieri, L. Rossi, Instrumentation of wildland fire: Characterisation of a fire spreading through a Mediterranean shrub, Fire Saf. J. 41 (2006) 171–184. https://doi.org/10.1016/j.firesaf.2005.11.010.
[13] D.R. Packham, Heat transfer above a small ground fire., Aust. For. Res. 5 (1970) 19–24.
[14] B.M. Wotton, J.S. Gould, W.L. McCaw, N.P. Cheney, S.W. Taylor, Flame temperature and residence time of fires in dry eucalypt forest, Int. J. Wildland Fire. 21 (2012) 270–281. https://doi.org/10.1071/WF10127.
[15] A. Trouvé, Y. Wang, Large eddy simulation of compartment fires, Int. J. Comput. Fluid Dyn. 24 (2010) 449–466. https://doi.org/10.1080/10618562.2010.541393.
[16] N. Ren, Y. Wang, S. Vilfayeau, A. Trouvé, Large eddy simulation of turbulent vertical wall fires supplied with gaseous fuel through porous burners, Combust. Flame. 169 (2016) 194–208. https://doi.org/10.1016/j.combustflame.2015.12.008.

[17] C. Lapointe, N.T. Wimer, J.F. Glusman, A.S. Makowiecki, J.W. Daily, G.B. Rieker, P.E. Hamlington, Efficient simulation of turbulent diffusion flames in OpenFOAM using adaptive mesh refinement, Fire Saf. J. 111 (2020) 102934. https://doi.org/10.1016/j.firesaf.2019.102934.
[18] J.F. Glusman, K.E. Niemeyer, A.S. Makowiecki, N.T. Wimer, C. Lapointe, G.B. Rieker, P.E. Hamlington, J.W. Daily, Reduced Gas-Phase Kinetic Models for Burning of Douglas Fir, Front. Mech. Eng. 5 (2019). https://doi.org/10.3389/fmech.2019.00040.
[19] S. McAllister, Critical mass flux for flaming ignition of wet wood, Fire Saf. J. 61 (2013) 200–206. https://doi.org/10.1016/j.firesaf.2013.09.002.
[20] A. Atreya, M. Abu-zaid, Effect Of Environmental Variables On Piloted Ignition, Fire Saf. Sci. 3 (1991) 177–186. https://doi.org/10.3801/iafss.fss.3-177.
[21] B. Moghtaderi, V. Novozhilov, D.F. Fletcher, J.H. Kent, A new correlation for bench-scale piloted ignition data of wood, Fire Saf. J. 29 (1997) 41–59. https://doi.org/10.1016/S0379-7112(97)00004-0.
[22] T. Harada, Time to ignition, heat release rate and fire endurance time of wood in cone calorimeter test, Fire Mater. 25 (2001) 161–167. https://doi.org/10.1002/fam.766.
[23] R.S. Parmar, M. Welling, M.O. Andreae, G. Helas, Water vapor release from biomass combustion, Atmospheric Chem. Phys. 8 (2008) 6147–6153. https://doi.org/10.5194/acp-8-6147-2008.
[24] S.C. Ferguson, A. Dahale, B. Shotorban, S. Mahalingam, D.R. Weise, The Role of Moisture on Combustion of Pyrolysis Gases in Wildland Fires, Combust. Sci. Technol. 185 (2013) 435–453. https://doi.org/10.1080/00102202.2012.726666.
[25] M.J. Spearpoint, J.G. Quintiere, Predicting the piloted ignition of wood in the cone calorimeter using an integral model — effect of species, grain orientation and heat flux, Fire Saf. J. 36 (2001) 391–415. https://doi.org/10.1016/S0379-7112(00)00055-2.
[26] P.J. Schroeder, R.J. Wright, S. Coburn, B. Sodergren, K.C. Cossel, S. Droste, G.W. Truong, E. Baumann, F.R. Giorgetta, I. Coddington, N.R. Newbury, G.B. Rieker, Dual frequency comb laser absorption spectroscopy in a 16 MW gas turbine exhaust, Proc. Combust. Inst. 36 (2017) 4565–4573. https://doi.org/10.1016/j.proci.2016.06.032.
[27] S. Coburn, C.B. Alden, R. Wright, K. Cossel, E. Baumann, G.-W. Truong, F. Giorgetta, C. Sweeney, N.R. Newbury, K. Prasad, I. Coddington, G.B. Rieker, Regional trace-gas source attribution using a field-deployed dual frequency comb spectrometer, Optica. 5 (2018) 320–327. https://doi.org/10.1364/OPTICA.5.000320.
[28] A.D. Draper, R.K. Cole, A.S. Makowiecki, J. Mohr, A. Zdanowicz, A. Marchese, N. Hoghooghi, G.B. Rieker, Broadband dual-frequency comb spectroscopy in a rapid compression machine, Opt. Express. 27 (2019) 10814–10825. https://doi.org/10.1364/OE.27.010814.
[29] T.R.S. Hayden, N. Malarich, D. Petrykowski, S.P. Nigam, J.D. Christopher, C. Lapointe, N.T. Wimer, P.E. Hamlington, G.B. Rieker, OH radical measurements in combustion environments using wavelength modulation spectroscopy and dual-frequency comb spectroscopy near 1491 nm, Appl. Phys. B. 125 (2019) 226. https://doi.org/10.1007/s00340-019-7341-6.
[30] R.J. Yokelson, D.W.T. Griffith, D.E. Ward, Open-path Fourier transform infrared studies of large-scale laboratory biomass fires, J. Geophys. Res. Atmospheres. 101 (1996) 21067–21080. https://doi.org/10.1029/96JD01800.

[31] R.J. Yokelson, J.G. Goode, D.E. Ward, R.A. Susott, R.E. Babbitt, D.D. Wade, I. Bertschi, D.W.T. Griffith, W.M. Hao, Emissions of formaldehyde, acetic acid, methanol, and other trace gases from biomass fires in North Carolina measured by airborne Fourier transform infrared spectroscopy, J. Geophys. Res. Atmospheres. 104 (1999) 30109–30125. https://doi.org/10.1029/1999JD900817.
[32] E.M. Waxman, K.C. Cossel, G.W. Truong, F.R. Giorgetta, W.C. Swann, S. Coburn, R.J. Wright, G.B. Rieker, I.R. Coddington, N.R. Newbury, Comparison of open-path dual frequency comb spectroscopy for high-precision atmospheric gas measurements, Atmospheric Meas. Tech. (2017). https://doi.org/922848.
[33] P.J. Schroeder, D.J. Pfotenhauer, J. Yang, F.R. Giorgetta, W.C. Swann, I. Coddington, N.R. Newbury, G.B. Rieker, High temperature comparison of the HITRAN2012 and HITEMP2010 water vapor absorption databases to frequency comb measurements, J. Quant. Spectrosc. Radiat. Transf. 203 (2017) 194–205. https://doi.org/10.1016/j.jqsrt.2017.04.023.
[34] P.J. Schroeder, M.J. Cich, J. Yang, F.R. Giorgetta, W.C. Swann, I. Coddington, N.R. Newbury, B.J. Drouin, G.B. Rieker, Speed-dependent Voigt lineshape parameter database from dual frequency comb measurements up to 1305 K. Part I: Pure H2O absorption, 6801–7188 cm−1, J. Quant. Spectrosc. Radiat. Transf. 210 (2018) 240–250. https://doi.org/10.1016/j.jqsrt.2018.02.025.
[35] L.S. Rothman, I.E. Gordon, Y. Babikov, A. Barbe, D. Chris Benner, P.F. Bernath, M. Birk, L. Bizzocchi, V. Boudon, L.R. Brown, A. Campargue, K. Chance, E.A. Cohen, L.H. Coudert, V.M. Devi, B.J. Drouin, A. Fayt, J.-M. Flaud, R.R. Gamache, J.J. Harrison, J.-M. Hartmann, C. Hill, J.T. Hodges, D. Jacquemart, A. Jolly, J. Lamouroux, R.J. Le Roy, G. Li, D.A. Long, O.M. Lyulin, C.J. Mackie, S.T. Massie, S. Mikhailenko, H.S.P. Müller, O.V. Naumenko, A.V. Nikitin, J. Orphal, V. Perevalov, A. Perrin, E.R. Polovtseva, C. Richard, M.A.H. Smith, E. Starikova, K. Sung, S. Tashkun, J. Tennyson, G.C. Toon, Vl.G. Tyuterev, G. Wagner, The HITRAN2012 molecular spectroscopic database, J. Quant. Spectrosc. Radiat. Transf. 130 (2013) 4–50. https://doi.org/10.1016/j.jqsrt.2013.07.002.
[36] L.R. Brown, C.M. Humphrey, R.R. Gamache, CO2-broadened water in the pure rotation and ν2 fundamental regions, J. Mol. Spectrosc. 246 (2007) 1–21. https://doi.org/10.1016/j.jms.2007.07.010.
[37] E. Ranzi, A. Cuoci, T. Faravelli, A. Frassoldati, G. Migliavacca, S. Pierucci, S. Sommariva, Chemical Kinetics of Biomass Pyrolysis, Energy Fuels. 22 (2008) 4292–4300. https://doi.org/10.1021/ef800551t.
[38] B. Dlugogorski, S. Hirunpraditkoon, E. Kennedy, Ignition Temperature and Surface Emissivity of Heterogeneous Loosely Packed Materials from Pyrometric Measurements, Fire Saf. Sci. 11 (2014) 262–275. https://doi.org/10.3801/IAFSS.FSS.11-262.
[39] Thermal model object - MATLAB, n.d. https://www.mathworks.com/help/pde/ug/pde.thermalmodel.html (accessed April 2, 2018).
[40] D.K. Shen, M.X. Fang, Z.Y. Luo, K.F. Cen, Modeling pyrolysis of wet wood under external heat flux, Fire Saf. J. 42 (2007) 210–217. https://doi.org/10.1016/j.firesaf.2006.09.001.
[41] V.D. Thi, M. Khelifa, M. El Ganaoui, Y. Rogaume, Finite element modelling of the pyrolysis of wet wood subjected to fire, Fire Saf. J. 81 (2016) 85–96. https://doi.org/10.1016/j.firesaf.2016.02.001.
[42] M.G. Grønli, M.C. Melaaen, Mathematical Model for Wood Pyrolysis Comparison of Experimental Measurements with Model Predictions, Energy Fuels. 14 (2000) 791–800. https://doi.org/10.1021/ef990176q.

[43] W.J. Parker, Prediction of The Heat Release Rate of Douglas Fir, Fire Saf. Sci. 2 (1989) 337–346. https://doi.org/10.3801/iafss.fss.2-337.
[44] F.P. Incropera, D.P. DeWitt, T.L. Bergman, A.S. Lavine, Fundamentals of Heat and Mass Transfer, 6th ed., John Wiley & Sons, 2007.
[45] H.E. Anderson, Heat transfer and fire spread, Res Pap INT-RP-69 Ogden Utah US Dep. Agric. For. Serv. Intermt. For. Range Exp. Stn. 20 P. 69 (1969). https://www.fs.usda.gov/treesearch/pubs/40489 (accessed March 2, 2020).
[46] K.M. Bryden, K.W. Ragland, C.J. Rutland, Modeling thermally thick pyrolysis of wood, Biomass Bioenergy. 22 (2002) 41–53. https://doi.org/10.1016/S0961-9534(01)00060-5.